Ultrasound in Med. & Biol., Vol. 39, No. 3, pp. 490–506, 2013

0301-5629/$ - see front matter

http://dx.doi.org/10.1016/j.ultrasmedbio.2012.09.025

● *Original Contribution*

SECONDARY BJERKNES FORCES DEFORM TARGETED MICROBUBBLES

Tom J. A. Kokhuis,*† Valeria Garbin,‡ Klazina Kooiman,* Benno A. Naaijkens,†§ Lynda J. M. Juffermans,†¶ Otto Kamp,†‖ Antonius F. W. van der Steen,*† Michel Versluis,# and Nico de Jong*†

*Biomedical Engineering, Thorax Center, Erasmus MC, Rotterdam, The Netherlands; †Interuniversity Cardiology Institute of the Netherlands, Utrecht, The Netherlands; ‡Department of Chemical Engineering, Imperial College London, London, UK; §Department of Pathology, VU University Medical Center, Amsterdam, The Netherlands; ¶Department of Physiology, VU University Medical Center, Amsterdam, The Netherlands; ‖Department of Cardiology, VU University Medical Center, Amsterdam, The Netherlands; and #Physics of Fluids Group and MIRA Institute of Biomedical Technology and Technical Medicine, University of Twente, Enschede, The Netherlands

(*Received* 8 *June* 2012; *revised* 24 *September* 2012; *in final form* 27 *September* 2012)

Abstract—In this study, we investigated the effect of secondary Bjerknes forces on targeted microbubbles using high-speed optical imaging. We observed that targeted microbubbles attached to an underlying surface and subject to secondary Bjerknes forces deform in the direction of their neighboring bubble, thereby tending toward a prolate shape. The deformation induces an elastic restoring force, causing the bubbles to recoil back to their equilibrium position; typically within 100 μs after low-intensity ultrasound application. The temporal dynamics of the recoil was modeled as a simple mass-spring system, from which a value for the effective spring constant k of the order 10^{-3} Nm^{-1} was obtained. Moreover, the translational dynamics of interacting targeted microbubbles was predicted by a hydrodynamic point particle model, including a value of the spring stiffness k of the very same order as derived experimentally from the recoiling curves. For higher acoustic pressures, secondary Bjerknes forces rupture the molecular adhesion of the bubbles to the surface. We used this mutual attraction to quantify the binding force between a single biotinylated microbubble and an avidin-coated surface, which was found to be between 0.9 and 2 nanonewtons (nN). The observation of patches of lipids left at the initial binding site suggests that lipid anchors are pulled out of the microbubble shell, rather than biotin molecules unbinding from avidin. Understanding the effect of ultrasound application on targeted microbubbles is crucial for further advances in the realm of molecular imaging. (E-mail: t.kokhuis@erasmusmc.nl) © **2013 World Federation for Ultrasound in Medicine & Biology.**

Key Words: **Targeted microbubbles, Secondary Bjerknes force, Acoustic radiation force, Binding force, Translational dynamics, Microbubble detachment, Bubble deformation, Lipid pullout, Ultrasound contrast agents, Molecular imaging.**

INTRODUCTION

Microbubbles are the most popular ultrasound contrast agent (UCA) used clinically for diagnostic ultrasound imaging. UCA microbubbles are typically 1–10 μm in size and consist of a gas core stabilized by a lipid, protein or polymer shell, which prevents coalescence with other bubbles and reduces dissolution. The microbubbles are contained in the circulatory system following intravenous administration until they are cleared by the reticuloendothelial system (Straub et al. 2007). Because of the compressibility of the gas core inside, the microbubbles undergo volumetric oscillations during ultrasound application, giving them superior echogenicity compared with the surrounding tissue and fluid. The higher echogenicity results in a better contrast-to-tissue ratio and is used in contrast-enhanced ultrasound imaging for enhanced tissue delineation, for perfusion studies or for left ventricle opacification (Dijkmans et al. 2004). Moreover, microbubbles have been shown to behave as non-linear ultrasound scatterers, causing their backscattered echo to contain higher harmonics (Burns et al. 1992; de Jong et al. 1994) or even subharmonics (Lotsberg et al. 1996; Sijl et al. 2010) of the driving frequency. The non-linear characteristics of

Address correspondence to: Tom J.A. Kokhuis, MSc, Erasmus MC, Department of Biomedical Engineering (Room Ee2302), PO Box 2040, 3000 CA Rotterdam, The Netherlands. E-mail: t.kokhuis@erasmusmc.nl

microbubbles are exploited in various imaging modalities, such as amplitude modulation (Mor-Avi et al. 2001) and pulse inversion (Simpson et al. 1999) to improve the contrast-to-tissue ratio.

In the mid 1990s, fabrication of the first so-called targeted microbubbles was reported, where ligands to specific molecular markers were added to the shell (Fritzsch et al. 1994; Klibanov et al. 1997). Ligands can be selected to make targeted microbubbles adhere to regions of the vascular endothelium expressing specific proteins, such as inflammatory markers. Imaging methods involving high-power destructive pulses can be used to discriminate between echoes originating from targeted and freely circulating bubbles (Willmann et al. 2008). More recently, it was shown that targeted microbubbles exhibit a pronounced shift (*i.e.*, a 50% decrease) in their frequency of maximum response compared with free bubbles (Overvelde et al. 2011). Although these experiments were performed in well-controlled model systems, their outcome suggests that acoustic discrimination between targeted and freely flowing bubbles is feasible.

The selective imaging of targeted microbubbles, in combination with their capability to recognize molecular events, facilitates targeted contrast enhancement during ultrasound application, also called *molecular ultrasound* (Deshpande et al. 2010). Molecular ultrasound has great potential to diagnose diseases in an earlier stage, such as in asymptomatic patients, and to assess treatment efficacy of drugs even before morphologic changes occur (Pysz et al. 2010). Recently, a new milestone was achieved when the first study of targeted microbubble imaging in humans was performed (Wijkstra et al. 2012). The Vascular Endothelial Growth Factor Receptor 2 (VEGF-R2) targeted microbubble BR55 (Bracco Research, Geneva, Switzerland) was shown to bind to VEGF-R2 receptors in the prostate of patients scheduled for prostatectomy, making molecular ultrasound potentially the first diagnostic imaging technique for prostate cancer detection and localization in the near future.

For molecular ultrasound to evolve to a robust diagnostic tool, more fundamental knowledge about the effects of ultrasound application on the behavior of targeted microbubbles is needed. This need is emphasized by the observations of Schmidt et al. (2008), who observed detachment and clustering of biotinylated microbubbles targeted to a avidin-coated surface during low intensity ultrasound application. Microbubble detachment reduces the amount of targeted microbubbles at the site of interest, decreasing the echo intensity and therefore complicating the interpretation of the signal. Clustering of microbubbles may change the echogenicity (Dayton et al. 1999; Doinikov et al. 2009). A correct interpretation of the molecular ultrasound signal therefore demands a thorough understanding of the interaction between ultrasound and targeted microbubbles.

The effects observed by (Schmidt et al. 2008) were ascribed to a mutual interaction between the oscillating microbubbles known as *secondary acoustic radiation force*. Because the direction of the pressure gradient (∇P) associated with a sound field emitted by a neighboring bubble oscillates in time, the secondary acoustic radiation force exerted on a bubble has alternating direction in time. However, as the volume (V) of the bubble also oscillates in time, the average of the instantaneous force over one period results in a net force, whose direction depends on the phase difference between the bubble oscillations and the oscillating pressure gradient (Leighton, 1994). This averaged net force is called *secondary Bjerknes force* (Bjerknes, 1906).

More recently, it was observed that targeted microbubbles, which had moved several hundred nanometers under the influence of attractive secondary Bjerknes forces, had moved back to their initial position by the start of a next experiment 80 ms after the ultrasound was turned off (Garbin et al. 2011). However, microbubbles that were in contact with (but not adherent to) the surface were reported to equilibrate at a new position, closer to each other. It was therefore hypothesized that the presence of an elastic restoring force brings the targeted microbubbles back to their equilibrium position after the ultrasound is turned off. The physical mechanism of this restoring force remained elusive: the extension associated with the stretching of molecular bonds is a few orders of magnitude smaller than the observed bubble translations. Moreover, bubbles remained spherical throughout the experiments. However, the authors did not totally rule out that bubble deformation might be involved because the induced deformation could have been below the optical resolution in top view. Furthermore, the formation of elastic wrinkles and folds of excess lipid material (Rychak et al. 2006), similar to what has been observed in neutrophil rolling in shear flow (Park et al. 2002), was proposed as a second possible mechanism of the restoring force.

In this study, we therefore investigated the phenomena associated with the translational dynamics of mutually interacting targeted microbubbles in more detail. We first repeated the experiments as performed by Garbin et al. (2011) for the different microbubbles and experimental configuration used in this study. Next, we investigated the time scale of the microbubble recoil after the ultrasound was turned off. To elucidate the mechanism of the elastic restoring force, simultaneous top and side-view high-speed imaging (Vos et al. 2011) of interacting targeted microbubbles was performed. The article concludes with a comparison between the experimental observations and theoretical predictions of the translational dynamics of interacting targeted bubbles

using a simplified hydrodynamic model and shows that rupturing the adhesion of targeted microbubbles using secondary Bjerknes forces has the potential to quantify the binding force of targeted microbubbles.

THEORETICAL FRAMEWORK AND NUMERICAL MODELING

Force balance during ultrasound application

We model the bubble translational dynamics during ultrasound application using a hydrodynamic model for two mutually interacting targeted microbubbles, pulsating in an ultrasound field (Garbin et al. 2011). The model is based on the equations of motion for mutually interacting bubbles in an unbounded fluid, which were shown to be in good agreement with experimental observations (Garbin et al. 2009). Because the targeted bubbles are in contact with a wall, the pressure gradient experienced by a bubble (owing to a pulsating neighboring bubble) is increased because of reflections from the wall. To account for this effect, the so-called method of images was applied in which the rigid wall is replaced by two so-called mirror bubbles, having the same size and oscillating with the same amplitude and phase as the original bubbles. This effectively results in an increase of the pressure gradient ∇P experienced by a bubble by a factor that equals the reflection coefficient of the material (Crum, 1975). The corresponding force balance, including all relevant forces, is reviewed below (see also Table 1 for a definition of the symbols used).

The total force balance along the line of centers (here defined as the x-axis) for a pulsating targeted bubble i, interacting with a neighboring bubble j, is given by:

$$\vec{F}_R+\vec{F}_{AM}+\vec{F}_{QS}+\vec{F}_H+\vec{F}_K=0 \tag{1}$$

where $\vec{F}_R$ is the secondary acoustic radiation force, which is driving the motion of bubble i. It arises because of the sound emitted by the neighboring microbubble j, when both bubbles are pulsating in an incident sound field (*i.e.*, the primary field). The instantaneous secondary acoustic radiation force acting on a microbubble can be calculated by using the general expression for radiation forces experienced by a body (Leighton, 1994):

$$F=-V\nabla P \tag{2}$$

where V is the volume and ∇P is the pressure gradient over the body.

By substituting V with the expression for the volume of bubble i, and ∇P with the pressure gradient generated by the pulsating neighboring microbubble j, with radius R_j, an expression for the instantaneous secondary acoustic radiation force on a targeted bubble i, with radius R_i can be derived:

$$\vec{F}_R=-(1+\beta)\rho_L\frac{4}{3}\pi R_i^3\frac{\ddot{R}_jR_j^2+2R_j\dot{R}_j^2}{d^2} \tag{3}$$

where ρ_L is the liquid density, d is the distance in between the two bubbles, R_i the radius of bubble i, R_j is the radius of bubble j, and $\dot{R}_j$ its first and $\ddot{R}_j$ its second time derivative. β is the reflection coefficient of the wall and accounts for the increase of the pressure gradient experienced by the bubble owing to wall reflections.

$\vec{F}_{AM}$ is the added mass force, which is due to the inertia of the liquid set into motion by an accelerating body. In the case of a bubble, the added mass force is much larger than the inertia of the gas (vapor) core of the bubble itself. For a bubble with time-dependent radius, the added-mass force is given by (Ohl et al. 2003):

$$\vec{F}_{AM}=-\frac{1}{2}\rho_L\left(V_i\frac{\partial\vec{U}_i}{\partial t}+\vec{U}_i\frac{\partial V_i}{\partial t}\right) \tag{4}$$

where V_i is the volume of bubble i and $\vec{U}_i=\dot{x}_i-\vec{u}$ is the velocity of the bubble relative to the fluid velocity $\vec{u}$.

$\vec{F}_{QS}$ is the quasi-steady viscous drag force. Because the coating of the microbubble enforces a no-slip boundary condition at the surface, the bubble experiences an increased drag compared with an uncoated bubble as a result of the generation of vorticity at the surface of the bubble. The quasi-steady drag is given, for small Reynolds numbers, by the Stokes drag (Landau and Lifshitz, 1987):

$$\vec{F}_{QS}=-6\pi\mu R_i\vec{U}_i \tag{5}$$

where μ is the dynamic fluid viscosity.

Moreover, because the motion of a bubble moving under the influence of acoustic radiation force includes a high-frequency component, the viscous drag experienced by the bubbles has an unsteady component in addition to the quasi-steady component (Garbin et al. 2009). The effect of the unsteady (high frequency) oscillatory translational motion can be understood by realizing that, for sufficiently high frequency of the oscillation, the bubble is continuously affected by the vorticity generated before by its own motion; this results in an increased drag experienced by that bubble. This effect is accounted for by the history force ($\vec{F}_H$), which for a no-slip bubble with time-dependent radius is given by (Takemura and Magnaudet, 2004):

$$\vec{F}_H=-6\pi\rho_L\sqrt{\frac{\nu}{\pi}}\int_0^t\frac{d\tau}{\sqrt{\int_\tau^t R_i(s)^{-2}ds}}\frac{d\left(R_i\vec{U}_i\right)}{dt} \tag{6}$$

where ν is the kinematic viscosity of the fluid.

Finally, to account for the observed recoil of targeted microbubbles after ultrasound insonification, we include a Hookean restoring force:

$$\vec{F}_K = -k\vec{x}_i \tag{7}$$

where k is the effective spring stiffness of the targeted bubble and $\vec{x}_i$ is the bubble displacement from its equilibrium position. The theoretical justification for this linear relationship between $\vec{F}_K$ and $\vec{x}_i$ is given in the Appendix.

When the bubble is bound to the functionalized surface, the sum of all the hydrodynamic forces acting on the bubble (defined as $\vec{F}_{Pull}$) should be opposed by the restoring force $\vec{F}_K$:

$$\vec{F}_R + \vec{F}_{AM} + \vec{F}_{QS} + \vec{F}_H = \vec{F}_{Pull} = -\vec{F}_K \tag{8}$$

Formulating eqn 1 for both bubbles gives two coupled second-order differential equations that were solved numerically to obtain the position of both bubbles $\vec{x}_i$ and $\vec{x}_j$ and the center-to-center distance d. The experimental radius-time curves ($R_i(t)$ and $R_j(t)$), their first derivatives ($\dot{R}_i(t)$ and $\dot{R}_j(t)$) and second derivatives ($\ddot{R}_i(t)$ and $\ddot{R}_j(t)$) were used as input parameters for the force balance. Buoyancy is not taken into account in the analysis because it acts in a direction orthogonal to the line of centers. Moreover, the mean terminal velocity of a buoyant bubble is a few orders of magnitude smaller than the motion driven by secondary acoustic radiation force and is therefore not relevant for the phenomena investigated in this study.

Force balance after ultrasound application

After the ultrasound is turned off, both the radial bubble oscillations and the oscillatory translations cease, and the secondary acoustic radiation force ($\vec{F}_R$) and history force ($\vec{F}_H$) are set to zero in the force balance of equation (1). Moreover, because the bubbles stop oscillating, the added mass force of equation (4) reduces to:

$$\vec{F}_{AM} = -\frac{1}{2}\rho_L V_i \frac{\partial \vec{U}_i}{\partial t} \tag{9}$$

The resulting force balance for each bubble after ultrasound application (*i.e.*, the recoil measurements) is therefore given by:

$$\vec{F}_{AM} + \vec{F}_{QS} + \vec{F}_K = 0 \tag{10}$$

The two resulting (now uncoupled) second-order differential equations were again solved numerically to obtain $\vec{x}_i$, $\vec{x}_j$ and the distance between the bubbles $d = |\vec{x}_i - \vec{x}_j|$.

Table 1. Notation force balance equation 1

Symbols	Force
$\vec{F}_R$	Secondary acoustic radiation force
$\vec{F}_{AM}$	Added mass force
$\vec{F}_{QS}$	Quasi-steady viscous drag force
$\vec{F}_H$	History force
$\vec{F}_K$	Restoring force

Theoretical predictions during and after ultrasound application

To obtain an estimate of the timescale of the recoil after ultrasound application, we solved the equation of motion (eqn [1]) with the radial dynamics predicted by the Marmottant model (Marmottant et al. 2005) as an input. The value for the shell viscosity (κ_s) was set to 5×10^{-8} kg/s, the value for the shell elasticity (χ) at 1 N/m and the initial surface tension ($\sigma(R_0)$) at 63 mN/m. All bubbles had a resting radius (R_0) of 2 μm. The theoretically predicted evolution of the separation distance between two bubbles (initially 10 μm apart) in response to 20 cycles at a frequency of 2.25 MHz at $P = 75$ kPa is shown in Figure 1. When the effective spring constant k is set to 0 (red curve), the bubbles approach each other during ultrasound application, but no recoil can be observed afterward. This situation represents the dynamics of two interacting non-targeted microbubbles. When a restoring term is included in the equation of motion (black curve, $k =$ 5 mN/m), the bubbles approach each other during ultrasound application (although significantly less than in the non-targeted case), but the separation distance is restored to the initial value of 10 μm within 20 μs after the ultrasound is turned off. The inset shows a close-up of the dynamics during the first 12 μs, including a few microseconds after ultrasound application. The start of the recoil is already visible for the targeted case (black curve). From these simulations, we can conclude that the recoil after ultrasound application is likely to cover several tens of microseconds, dependent on the stiffness of the effective spring constant k. To capture the recoil, we therefore imaged the interacting bubbles at relatively low frame rates (1 million frames per second (Mfps)). In this way, we covered a time window lasting more than 100 μs. Experimentally, it was observed that a higher pressure was needed to translate the bubbles. Both the vicinity of a wall and neighboring bubbles are known to suppress the oscillation amplitude (Garbin et al. 2007), which will also influence the observed translation of the bubbles. This motivated us to use the

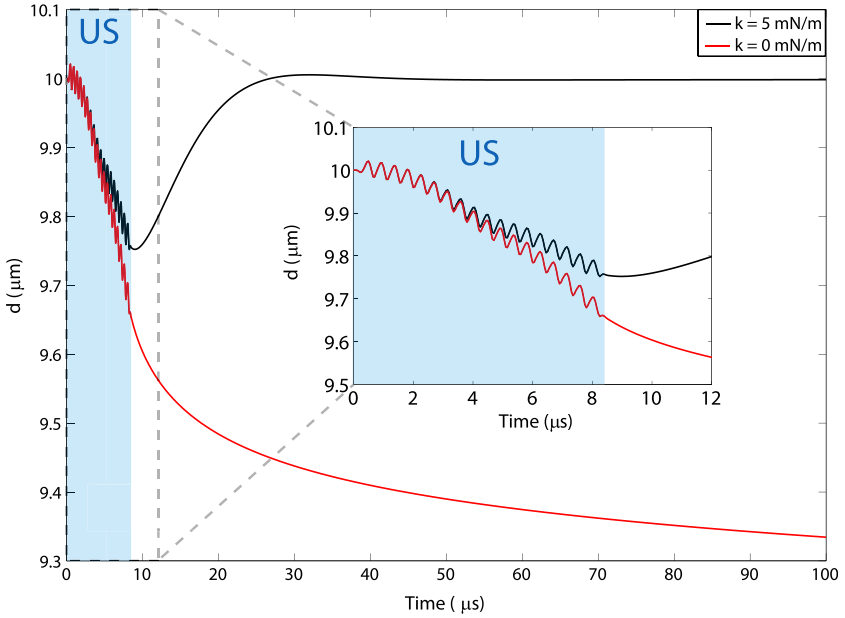

Fig. 1. Simulated distance between two microbubbles during and after insonification with an ultrasound wave of 20 cycles at a frequency of 2.25 MHz (P = 75 kPa). The time span of ultrasound application is indicated by the marked area. The black curve corresponds to targeted microbubbles (both with an effective spring constant k of 5 mN/m). The red curve corresponds to two bubbles in contact with (but not adherent to) a rigid wall (*i.e.*, k = 0 mN/m). The inset shows a close-up of the first 12 μs. In contrast to the non-targeted bubbles, the start of recoil is already visible for the targeted bubble pair. The resting radius of both bubbles was 2 μm.

experimentally obtained radius-time curves (and its derivatives) as input parameters for the hydrodynamic model to compare simulations and experiment.

MATERIALS AND METHODS

Preparation of microbubbles

Biotinylated microbubbles with a perfluorobutane (C_4F_{10}) gas core were made by sonication (Klibanov et al. 2004). The mean diameter of the microbubble distribution was 3.5–4.0 μm. The coating was composed of 1,2-distearyol-*sn*-glycero-3-phosphocholine (59.4 mol %; P 6517; Sigma-Aldrich, Zwijndrecht, the Netherlands), polyoxyethylene-40 stearate (35.7 mol %; P 3440; Sigma-Aldrich), 1,2-distearyol-*sn*-glycero-3-phosphoethanolamine-N-[methoxy(polyethylene glycol)2000] (DSPE-PEG(2000); 4.1 mol %; 880125 P; Avanti Polar Lipids, Alabaster, AL, USA) and DSPE-PEG(2000)-biotin (0.8 mol %; 880129 C; Avanti Polar Lipids). For fluorescence microscopy, a very small amount of the lipophilic dye octadecyl-indocarbocyanine (DiI; Molecular Probes, Eugene, OR, USA) was dissolved in ethanol and added to the solution just before sonication.

OptiCell coating

For top-view experiments, the topside of an OptiCell (Thermo Fisher Scientific, Waltham, MA, USA), consisting of two 75-μm–thick polystyrene membranes separated by 2 mm, served as a target surface and was coated with NeutrAvidin (Life Technologies Europe, Bleiswijk, The Netherlands). A 100-μL droplet of 1 μg/mL solution of NeutrAvidin in phosphate-buffered saline (PBS; Life Technologies Europe) was deposited on an OptiCell membrane and incubated overnight at room temperature in a humidity chamber. As a negative control, a 100-μL droplet of PBS was used. After 24 hours, the surface was rinsed with PBS to remove all the unbound protein and incubated for 1 h with 1% bovine serum albumin (Sigma-Aldrich) to prevent unspecific binding. Afterward, the surface was rinsed again with PBS and mounted with the coated side down in a tank filled with PBS. Biotinylated microbubbles were injected in the tank and allowed to interact with the coated surface by flotation for 10 minutes. Afterward, the surface was again rinsed with PBS to remove all unbounded microbubbles, and the bottom (non-coated) membrane was cut from the OptiCell. Following these preparation steps, the OptiCell with the targeted bubbles was mounted on top of a tank filled with gas-saturated water with the targeted microbubbles on top. The targeted microbubbles, separated by the thin remaining polystyrene surface of the OptiCell from the water below, were submerged in PBS.

Capillary coating

For simultaneous top- and side-view imaging of targeted microbubbles, a polystyrene capillary (Paradigm

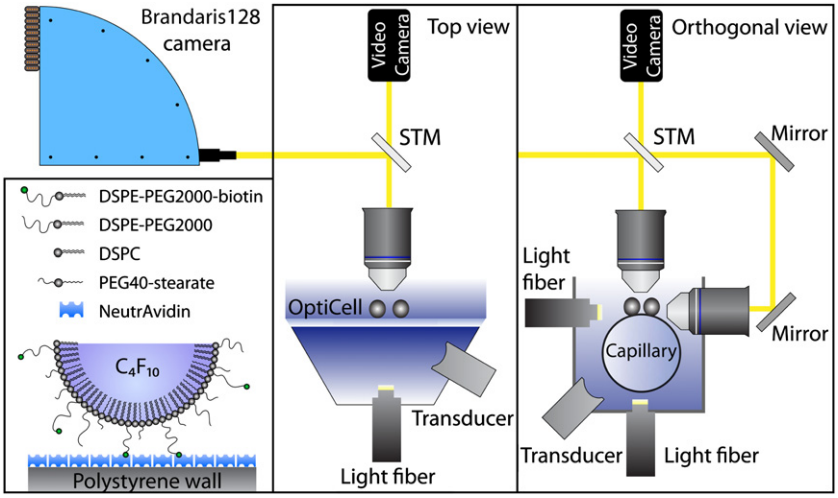

Fig. 2. Schematic drawing of the experimental setup used for top-view and orthogonal-view high-speed imaging. In the orthogonal configuration, the optical pathways of top and side view are merged after passing the semi-transparent mirror. The bottom left panel shows a schematic representation of the bubble shell and the target surface.

Optics Inc., Vancouver, WA, USA), with inner and outer diameters of 15 and 80 μm, respectively, was used as target surface. The capillary was submerged in a 1 μg/ml solution of NeutrAvidin and incubated overnight at room temperature. The surface was then rinsed with PBS and incubated for 1 h with 1% bovine serum albumin. After rinsing with PBS, the capillary was mounted in a tank. The tank was filled with PBS, and the bubbles were injected. Next, the fluid level was decreased so that the bubbles were in contact with the top side of the capillary. After 10 minutes, the fluid level was again increased and the chamber was rinsed several times with PBS to remove unbound bubbles from the solution.

Experimental setup

Figure 2 shows a schematic representation of the experimental setups used for top- and orthogonal-view (*i.e.*, simultaneous top and side view) high-speed imaging. For top-view imaging, the OptiCell was mounted on a water tank that also held an illumination fiber and a 2.25-MHz single element PZT transducer (Panametrics Inc., Waltham, MA, USA) with a focal distance of 75 mm. A semi-transparent mirror was used to split the transmitted light into a part to the Brandaris 128 camera (Chin et al. 2003) and a part to a high-sensitivity charge-coupled device (CCD) video camera (Watec LCL 902K; Watec Inc., Middletown, NY, USA). Microbubbles were imaged with a customized BXFM microscope (Olympus Nederland B.V., Zoeterwoude, the Netherlands) equipped with a 2× magnification ring in combination with a 60× water-immersion objective lens (LUMPLFL, numerical aperture (NA) = 0.9; Olympus) or a 100× water-immersion objective lens (LUMPLFL, NA = 1.0; Olympus). Fluorescence (DiI) was visualized using a fluorescence illuminator containing a 100-W mercury lamp (U-LH100HG) in combination with a fluorescence cube (U-MWG2; excitation 510–550 nm, emission 590 nm, dichroic filter 570 nm; Olympus). Fluorescence images were captured before and after ultrasound application.

The setup used for orthogonal imaging allows for the placement of an additional objective lens orthogonal to the top view lens (Vos et al. 2011). Because of the restrictions in space when using two objective lenses positioned orthogonally, the imaging was performed with two 40× water-immersion objective lenses (LUMPLFL, NA = 0.8; Olympus). Collimated light beams from the side-view objective were redirected by two mirrors and merged with the beams originating from the top-view objective using a semi-transparent mirror. Part of the combined image was directed to the Brandaris 128 camera, and part was directed to the CCD camera. The water tank held two light fibers and a focused polyvinylidene fluoride (PVDF) transducer (PA076; Precision Acoustics, Dorchester, UK) with a focal distance of 25 mm.

Microbubbles were insonified at varying pressures (P = 0–330 kPa) with 20–30 cycles with a Gaussian tapered window at a frequency of 2.25 MHz, generated by an arbitrary waveform generator (Model 8026; Tabor Electronics Ltd., Tel Hanan, Israel) and amplified by a 60-dB radiofrequency linear amplifier (Model A-500; ENI, Rochester, NY, USA). The optical and acoustical foci were aligned before each experiment. The transducers were calibrated using a 0.2-mm PVDF probe hydrophone (Precision Acoustics) in combination with a motorized xyz-stage controlled by MATLAB (Mathworks, Natick, MA, USA). The bottom left panel of Figure 2 shows the position of the targeted bubbles with

respect to the functionalized substrate. In both the top-view and the orthogonal-view experiments, targeted microbubbles were positioned on top of the polystyrene membrane. In this configuration, microbubbles that were not bound to the surface would float out of the optical focus because of buoyancy.

High-speed imaging protocol

For high-speed imaging purposes, images were relayed to the ultrafast-framing Brandaris 128 camera. Because of the differences in time scale of the dynamics during and after ultrasound application (Fig. 1), different imaging protocols were used to capture the translation dynamics during and after ultrasound application. To capture the translational dynamics after ultrasound insonification, frame rates near 1 Mfps were used. This resulted in a time window of the order of 100 μs for each individual movie consisting of 128 frames, sufficient to capture the entire recoiling phase. The first 10 μs of these movies captured the oscillatory attraction (but undersampled) and the remaining part captured the recoil of the microbubbles. To study the translation dynamics during ultrasound application, higher frame rates were used (typically $\sim$11 Mfps), resulting in a time window of $\sim$12 μs for each individual movie of 128 frames. The time between consecutive movies was 80 ms. The movies were transferred to a computer and analyzed offline.

Data analysis

The radius and center of mass of the microbubbles in each frame was determined by using semi-automatic custom software written in MATLAB (van der Meer et al. 2007). The determination of the absolute position of the bubbles is affected by microscopic misalignments of the individual sensors of the Brandaris 128 camera in regard to the optical axis. We compensated for this effect using calibration grids. After compensation, the maximum variation in the absolute bubble position was typically 80–130 nm. The center-center distance is not affected by this effect and was therefore considered to be the most reliable measure of displacement. The maximum variation in the center-to-center distance observed before ultrasound application was typically 60–90 nm. For the radius of the bubbles, this variation was typically 30–50 nm. The radius-time curves and the distance-time curves obtained experimentally were resampled using a cubic interpolation. The semi-automatic contour-tracking software failed to track the contour of the bubbles in side view because of a lack of contrast close to the capillary. We therefore tracked the contour of the bubbles in these images manually (in both top and side views). The semi-major and semi-minor axes were determined using the MATLAB routine "regionprops."

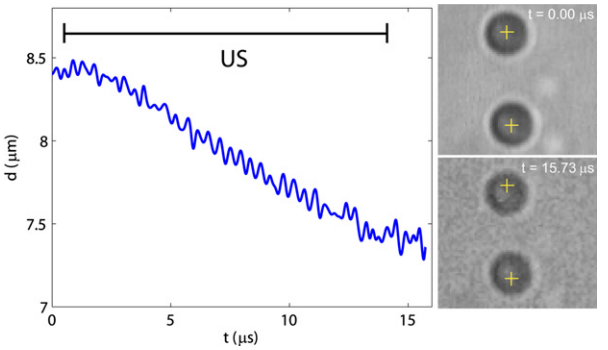

Fig. 3. The distance between two targeted microbubbles during insonification with 30 cycles at a frequency of 2.25 MHz (P = 250 kPa). The black bar corresponds to the time window of ultrasound application. The ring-down of the transducer and transient behavior of the microbubbles causes the oscillations to continue for a few more cycles after the driving pulse ends. The two snapshots on the right correspond to the configuration before (t = 0 μs) and immediately after application of ultrasound (t = 15.73 μs). The yellow crosshairs indicate the position of the centers of mass of the bubbles at t = 0 μs. The resting radius of both bubbles was 2 μm. See also Video 1 online.

RESULTS

Translational dynamics during ultrasound application

Targeted microbubbles of similar size were observed to be mutually attracted to each other during ultrasound application. Figure 3 shows the evolution of the center-to-center distance between two targeted bubbles insonified with 30 cycles at a frequency of 2.25 MHz and P = 250 kPa. The typical high-frequency oscillation (at the applied ultrasound frequency), owing to the alternating attractive and repulsive character of the secondary acoustic radiation force superimposed onto a slow drift toward each other, can be observed.

Although the center-to-center distance decreased by 1 μm during ultrasound application, no apparent bubble deformation was visible in top view. The two snapshots on the right side of Figure 3 correspond to the configuration before (t = 0 μs) and immediately after ultrasound application (t = 15.73 μs). The yellow crosshairs correspond to the positions of the centers of the bubbles at t = 0 μs, just before ultrasound application. Immediately after ultrasound application, the center of each bubble is shifted along the line of centers in the direction of the other bubble.

At relatively low acoustic pressures, targeted microbubbles exhibit spring-like behavior. Microbubbles moved toward each other during ultrasound application, but recoiled back to their initial position afterward.

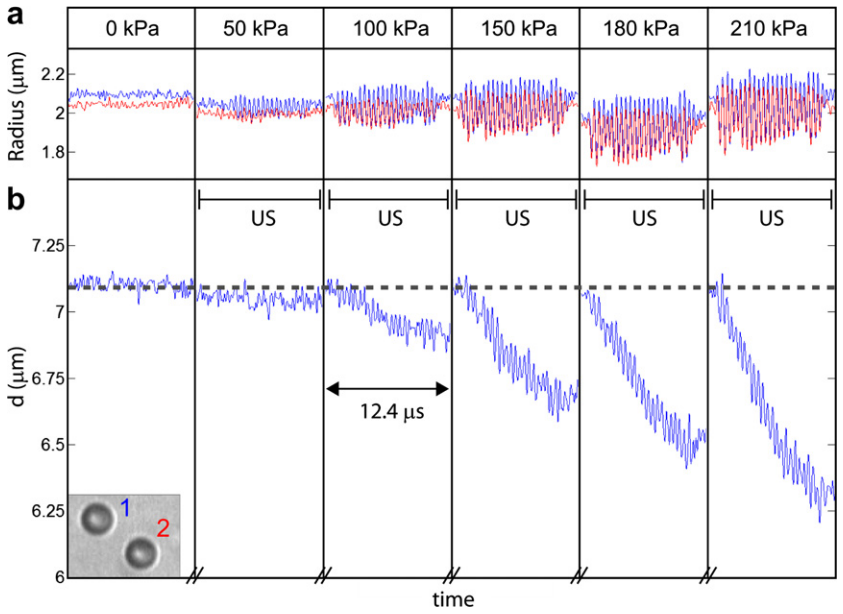

Fig. 4. (a) Radius-time curve of the two bubbles shown in the inset (blue for bubble 1, red for bubble 2) during six successive experiments (20 cycles at a frequency of 2.25 MHz, P = 0–210 kPa). No ultrasound was applied in the first experiment. (b) Center-to-center distance during the six successive experiments. The time span of one individual experiment was 12.4 μs. The vertical lines indicate the time gap of 80 ms between the successive experiments. The black bars correspond to the time windows of ultrasound application. The resting radius of both bubbles was approximately 2 μm (see also the R-t curves in panel (a)).

Figure 4 shows six successive experiments in which two targeted microbubbles (see inset) were insonified with 20 cycles at a frequency of 2.25 MHz at various acoustic pressures up to P = 210 kPa. For each individual experiment, with a time span of 12.4 μs, the top panel shows the radial excursions of the two microbubbles (blue for

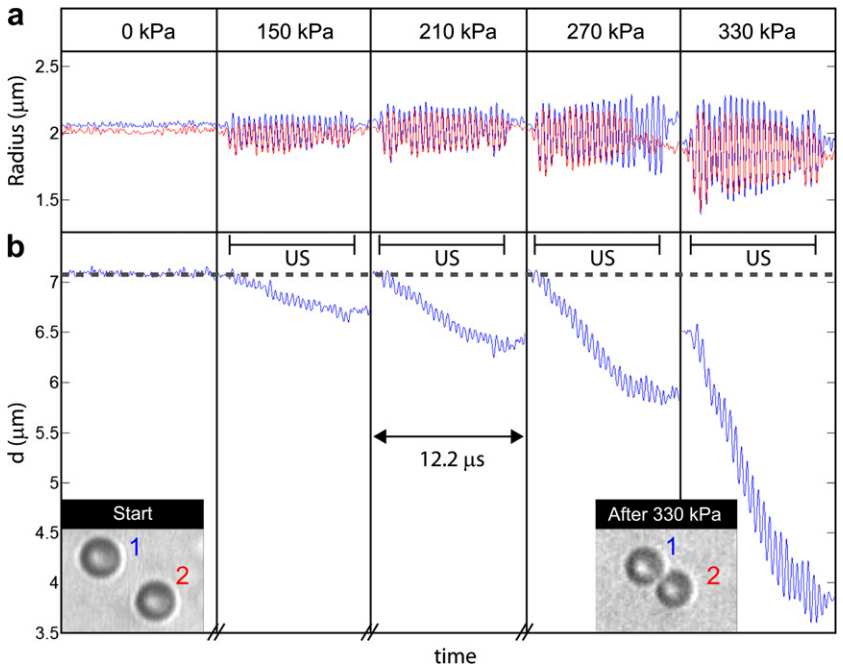

Fig. 5. Microbubbles of Figure 4 insonified in a second experiment at higher pressures up to P = 330 kPa. (a) Radius time curve (blue for bubble 1, red for bubble 2) during successive experiments. (b) Evolution of the center-to-center distance during the five experiments. The time span of one individual experiment was 12.2 μs. The left and right insets represent the initial and final bubble positions, respectively.

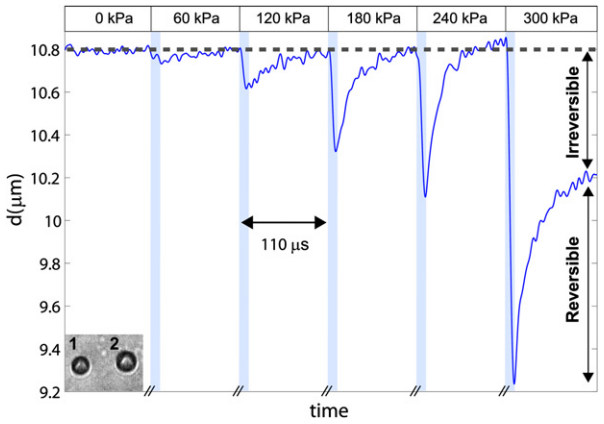

Fig. 6. Distance between two targeted microbubbles (displayed in the inset) versus time during and after ultrasound insonification. The pressure was increased in subsequent experiments (P = 0–300 kPa). The time span between the experiments was 80 ms. Bubbles were insonified at the start of each experiment with 20 cycles at a frequency of 2.25 MHz (indicated by the light blue blocks), lasting for ~9 μs. The total time covered by each movie was 110 μs. The resting radii of bubble 1 and bubble 2 were 2.2 and 2.4 μm, respectively.

bubble 1, red for bubble 2), and the bottom panel shows the evolution of the center-to-center distance. The vertical lines indicate the position of the time gap between consecutive experiments, which was set at 80 ms. No ultrasound was applied in the first movie. The center-to-center distance was observed to decrease during ultrasound application as observed before, because of an attractive secondary Bjerknes force. However, by the start of a successive experiment (*i.e.*, 80 ms after the ultrasound was turned off) the distance had again recovered to the initial value of 7.1 μm, implying the presence of a restoring store, causing each bubble to move back to its original position. These jumps in the center-to-center distance between successive experiments were not observed during control experiments with biotinylated microbubbles in contact with an uncoated OptiCell membrane. In that case, the distance in between two microbubbles did not recover to the initial value after ultrasound application.

To investigate the possibility of detaching the targeted microbubbles using this attractive secondary Bjerknes force, the same bubbles were insonified at higher pressure in the range of 0–330 kPa. The radius time curves (top panel) and center-center distance-time curves (bottom panel) are shown in Figure 5. Following insonification until a pressure of 210 kPa (*i.e.*, a distance decrease of 700 nm), the bubbles were still observed to move back to their initial position afterward. However, after insonification of the microbubbles with 270 kPa (*i.e.*, a distance decrease of 1.3 μm), the distance restored only partially to the new value of 6.5 μm, suggesting the adhesion of at least one bubble to the substrate was broken. At the end of the fifth experiment (P = 330 kPa), the microbubbles were in contact with each other and the center-to-center distance had reduced to a value equal to the sum of both radii. Remarkably, bubble 2 exhibited a sudden decrease in pulsation amplitude during the 270-kPa experiment. This phenomenon was observed before with two interacting bubbles positioned away from a wall (Garbin et al. 2007) and is expected to result from complex bubble-bubble interactions in close proximity. The initial and final positions of the two bubbles are shown in the left and right inset, respectively. After the experiment, both bubbles were observed to be smaller in size. The loss of shell material as a result of lipid pullout owing to microbubble detachment (which will be discussed later) might have accelerated the shrinkage of the bubbles because of the increased Laplace pressure.

Translational dynamics after ultrasound application

Between successive insonifications at relatively low pressures (Fig. 4), it was observed that microbubbles had moved back to their initial position. To capture the entire translation after ultrasound application (*i.e.*, when radial pulsations had ceased), microbubbles were insonified with 20 cycles at 2.25 MHz and imaged at a relatively low frame rate (1.15 Mfps). The results of six successive experiments at various acoustic pressures are shown in Figure 6. Each individual experiment covered a time window of 110 μs. Microbubbles were insonified during the first part of each movie with 20 cycles at a frequency of 2.25 MHz, indicated by the blue transparent windows in Figure 6. The remaining part of the movies captured the relaxation of the microbubbles afterward. As observed before, the center-to-center distance decreased during ultrasound application, clearly visible for the 180-, 240- and 300-kPa experiments shown in Figure 6. At the moment the ultrasound was turned off, the distance reached a minimum value (10.3, 10.1 and 9.2 μm for the 180-, 240- and 300-kPa experiment, respectively). After insonification with 180 and 240 kPa, the distance was observed to recover to the initial value of 10.8 μm within 100 μs. A small overshoot during the last part of the 240 kPa movie was also observed. Insonification with a pressure of 300 kPa resulted in only a partial recovery of the center-to-center distance which equilibrated around a new value of 10.2 μm instead. Again, no bubble deformation could be observed in top view. A closer inspection revealed that only bubble 1 had detached from its initial binding position after insonification with 300 kPa; bubble 2 had moved back to its initial position. The 1.6-μm decrease in center-to-center distance during insonification with 300 kPa is therefore the sum of a reversible component and irreversible component (arrows in Fig. 6). The irreversible component (0.6 μm) is due to unbinding of bubble 1 from the functionalized

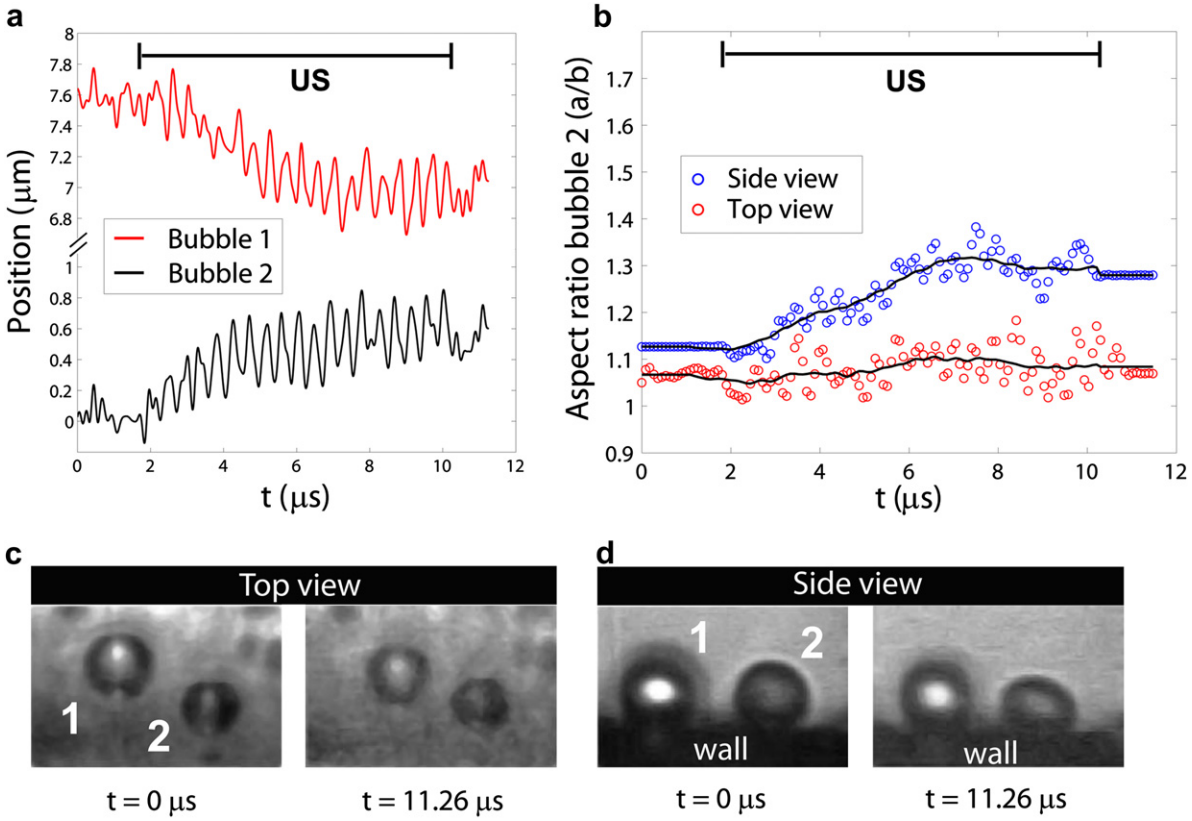

Fig. 7. (a) The effect of the secondary Bjerknes force on the individual position of two neighboring targeted bubbles seen in top view. The bubbles were insonified with 20 cycles (P = 153 kPa) at a frequency of 2.25 MHz. The resting radii of bubbles 1 and 2 were 2.5 and 2.2 μm, respectively. (b) The aspect ratio (a:b, with a as the semi-major and b as the semi-minor axis) of bubble 2 in top view (red dots) and in side view (blue dots) during the same experiment. (c) Top-view images of both bubbles before (t = 0 μs) and immediately after ultrasound application (t = 11.26 μs). (d) Side-view images of the same bubbles before (t = 0 μs) and right after ultrasound application (t = 11.26 μs).

substrate. The reversible component (1 μm) is equal to the sum of the backward translation of both bubbles afterwards (*i.e.*, bubble 1 was not completely detached), driven by the restoring force F_K.

Mechanism of the restoring force

To elucidate the mechanism of the restoring force causing the targeted microbubbles to recoil to their initial position after the ultrasound is turned off, the dynamics of the bubbles were imaged simultaneously in top and side views. The bubbles were positioned on top of a polystyrene capillary coated with NeutrAvidin and were insonified with 20 cycles at a frequency of 2.25 MHz. The results are shown in Figure 7a, which shows the effect of the attractive secondary Bjerknes force on the position of two neighboring bubbles seen in the top view. The resting radii of bubbles 1 and 2 were 2.5 and 2.2 μm, respectively. The initial position of bubble 1 was set to the initial separation distance of 7.6 μm; the initial position of bubble 2 was set to 0 μm. Attractive secondary Bjerknes forces caused both bubbles to move by ~600 nm along the line of centers toward the other bubble. No apparent deformation was visible in top view, confirming earlier observations. However, side-view imaging revealed that a microbubble elongates in the direction of the other bubble, thereby tending toward a prolate shape. This effect is illustrated for the in-focus bubble 2 in Figure 7b. The aspect ratio of the bubble in top view (red dots) is approximately constant and near unity throughout the experiment. However, the aspect ratio in side view (blue dots) increases by ~ 20%, from 1.1 before to 1.3 immediately after ultrasound application. Figure 7 (c, d) shows the top-view and side-view images of the same bubbles, before (t = 0 μs) and immediately after ultrasound application (t = 11.26 μs). The deformation of bubble 2 is clearly visible. The black area at the bottom of the side-view images represents the wall of the top side of the capillary. Please note that because the line of centers was not completely parallel to the object plane of the side view objective, only bubble 2 appears to be in focus in side view; bubble 1 appears to be slightly out of focus. We have therefore directed the side view analysis on bubble 2 only.

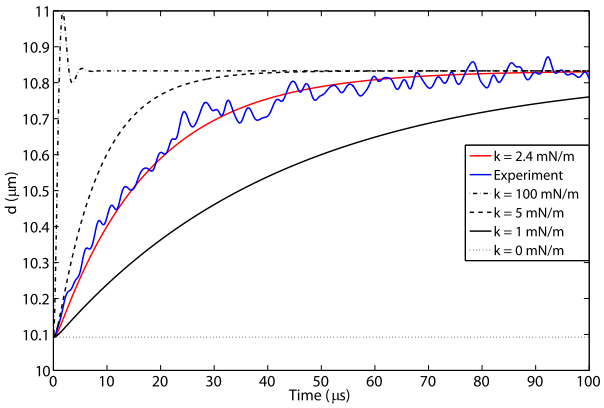

Fig. 8. Center-to-center distance between two targeted microbubbles versus time after insonification with 20 cycles at a pressure of 240 kPa. Here, $t = 0$ μs corresponds to the time the ultrasound was turned off. Shown here are the experimental data (blue curve) and simulated curves for different values of k. A value of $k = 2.4$ mN/m (red curve) gave the best fit between theory and experiment ($r^2 = 0.98$). The simulated curves for $k = 100$ mN/m (dash-dotted black line), $k = 5$ mN/m (dashed black line), $k = 1$ mN/m (solid black line) and $k = 0$ mN/m (dotted black line) are also shown for comparison.

These results show that microbubbles subjected to an attractive secondary Bjerknes force tend to deform toward a prolate spheroid in the direction of the other bubble. This deformation induces a restoring force $\vec{F}_K$ that opposes the net pulling force F_{Pull}, up to a point where it overcomes the adhesion force of the microbubble to the substrate and the bubble detaches.

Effective spring constant k

For small displacements (typically less than ~500 nm for the microbubble sizes studied here; $R_0 = 2$–2.5 μm), the restoring force causes the microbubbles to move back to their initial positions within 100 μs after the ultrasound is turned off. To quantify the value of the effective spring stiffness k, the theoretical prediction of the center-to-center distance obtained by solving the equation of motion after ultrasound application (eqn [10]) was fitted to the experimental data. The experimental result of the 240-kPa experiment of Figure 6 is shown again in Figure 8 (blue curve). Only the relaxation part is shown in Figure 8, and the curve starts when the center-to-center distance was at the minimum value of 10.1 μm (*i.e.*, $t = 0$ μs corresponds to the time the ultrasound was turned off). Using a least-squares fitting, a value of $k = 2.4$ mN/m was obtained for the spring stiffness (red curve, $r^2 = 0.98$). Theoretical predictions for $k = 100$ mN/m (dash-dotted black line), $k = 5$ mN/m (dashed black line), $k = 1$ mN/m (solid black line) and $k = 0$ mN/m (dotted black line) are also plotted. The solution for $k = 100$ mN/m gives a clear overshoot and subsequent ringing, which is characteristic for the relaxation of an underdamped harmonic oscillator. The experimental observation clearly resembles an overdamped situation. As expected, when $k = 0$ mN/m (*i.e.*, no restoring force present), there is no recovery of the initial distance after the ultrasound is turned off.

Modeling translational dynamics during ultrasound application

Garbin et al. (2011) showed that the translational dynamics of mutually interacting microbubbles, in contact with but not adherent to a polystyrene wall, can be predicted with a hydrodynamic point particle model. We modify the model by the addition of a restoring term $\vec{F}_K$ and extract a value of the effective spring constant by fitting the experimental data during ultrasound application.

The results are shown in Figure 9. The blue curve shows the experimentally obtained distance-time curve between two targeted microbubbles during insonification with 20 cycles at 2.25 MHz and $P = 210$ kPa. Not including a restoring term (*i.e.*, $k = 0$) in the force balance leads to an overestimation of the decrease in the separation distance by ~600 nm (see red curve). However, including a restoring term in the force balance, with a value of $k = 6$ mN/m gives a good prediction of the final separation distance (see black curve). Moreover, the agreement during the high-frequency oscillatory part is also satisfactory. Furthermore, the beginning of the recoil (after ultrasound) is also predicted by the model. The value of $k = 6$ mN/m is of the same order as that derived independently from the recoiling curves for a different set of bubbles, and which amounted to 2.4 mN/m (see previous section).

Quantification of the microbubble binding force

In the previous sections we have shown that above a certain threshold of the displacement, microbubbles did not move back anymore to their initial position, suggesting that the bubbles had (partially) detached from their initial position at the functionalized substrate. We hypothesize that a microbubble detaches from the substrate when the restoring force $\vec{F}_K$, opposing the net pulling force, exceeds the cumulative force that the adhesive belt of the microbubble can resist. To estimate this force, the value of the effective spring constant (k) and the distance translated by the center of mass of the bubbles ($\vec{x}$) needs to be known. The value of the effective spring constant k can be deduced from the recoiling curves like the ones shown in Figure 6. For the bubble pair of Figure 6, a value for the effective spring constant k of 2.4 mN/m was obtained (Figure 8). From Figure 6 we can also conclude that the bubbles still moved back to their initial position after a decrease in distance of 0.7

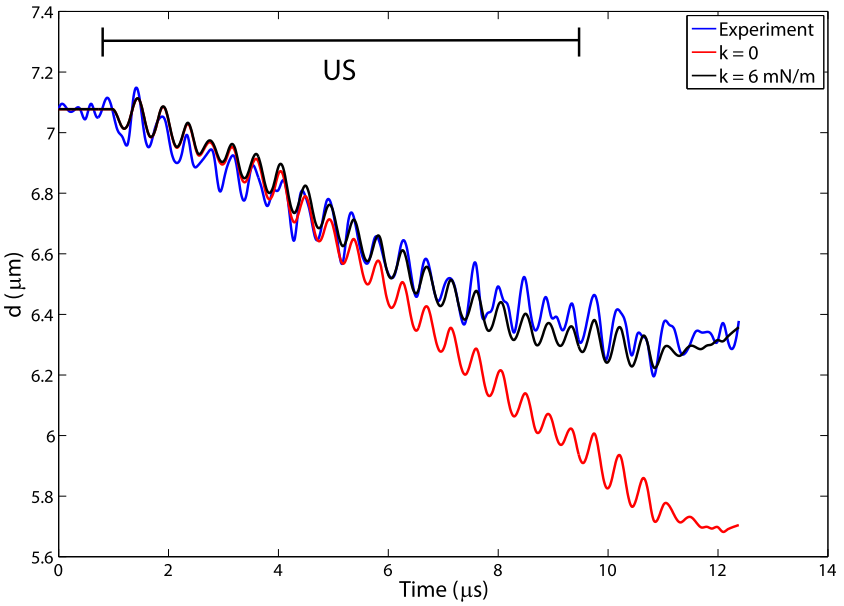

Fig. 9. The blue curve shows the distance in between two targeted microbubbles during insonification with 20 cycles at a frequency of 2.25 MHz and $P = 210$ kPa. The red curve shows the predicted curve by the hydrodynamic model with $k = 0$ mN/m. The black curve shows the prediction by the model with $k = 6$ mN/m. The time span of ultrasound application is indicated by the black bar.

μm (*i.e.*, 0.35 μm translation per bubble) because of insonification with 20 cycles at 2.25 MHz and $P = 240$ kPa. However, after a decrease of 1.6 μm (*i.e.,* 0.80 μm of translation per bubble), the center-to-center distance only recovered partially and was observed to equilibrate at the new value of 10.2 μm. Although both bubbles were observed to translate equally during ultrasound application, only bubble 1 (*i.e.*, the smaller bubble) had detached from the substrate during the experiment at $P = 300$ kPa. Presumably, because of it smaller contact area, the smaller bubble 1 has fewer molecular interactions with the target surface, making it the weakest link of this bubble pair. By multiplying the value of k with the experimentally observed translation of the bubble during the 240- and 300-kPa experiments, we can estimate the lower and upper limits of the force that the adhesive belt of the bubble can resist. For bubble 1, this threshold force was calculated to be 0.9–2.0 nN. Because bubble 2 still moved back to its initial position after insonification with 300 kPa, we can conclude that the threshold force to initiate detachment for this particular bubble was not exceeded at this pressure level.

DISCUSSION

We studied the translational dynamics of mutually interacting targeted microbubbles during and after ultrasound application in detail using high-speed optical imaging. Targeted microbubbles of similar size were observed to attract each other during ultrasound application. Typically, this movement consists of a high frequency component equal to the frequency of the applied sound superimposed onto a slow drift towards each other (see Figs. 3 and 9). In contrast to non-targeted microbubbles in contact with a wall, targeted microbubbles were observed to have moved back to their initial starting position by the start of the next experiment

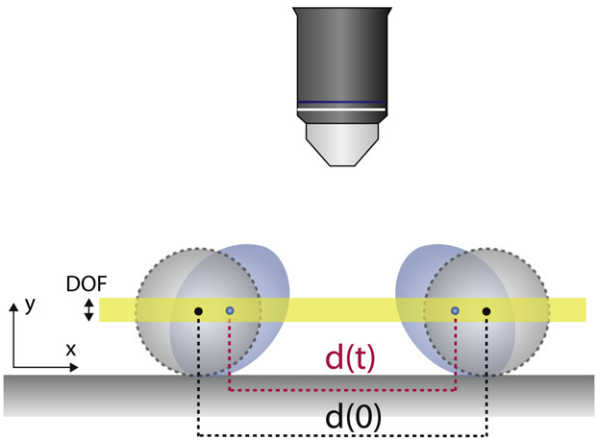

Figure 10. Artist's impression of the deformation of two targeted microbubbles during ultrasound application. The reader is looking through the side-view objective. The initial position of the center of mass of both bubbles (grey circles) is indicated by the black dots. The position of the center of mass of the two deformed bubbles (blue spheroids) during ultrasound application at time point t is indicated by the blue dots. The depth of field of the top view objective lens is indicated by the yellow bar (~800–1000 nm for the imaging system used in this study).

80 ms later (Garbin et al. 2011). The presence of a restoring force $\vec{F}_k$ was therefore already hypothesized by the previous authors. In this study, we imaged the recoil of targeted microbubbles under the influence of this restoring force after the ultrasound was turned off. Simultaneous top- and side- view high-speed imaging revealed that during ultrasound application, a targeted microbubble deforms in the direction of its neighboring bubble, tending toward a prolate shape (see side-view image at $t = 11.26$ μs; Fig. 7). The simultaneously obtained top-view recordings did not, however, exhibit bubble deformation, confirming earlier observations.

The apparent contradiction between top- and side-view observations (deformation vs. no deformation) can be explained by the orientation of the corresponding object planes of the top- and side-view objectives. Figure 10 shows an artist's impression (not to scale) of the deformation of interacting targeted microbubbles during ultrasound application. The reader is looking through the side-view objective. The grey circles represent the initial configuration. When the ultrasound is turned on, mutual attractive interactions cause the bubbles to bend over into the direction of the neighboring bubble, inducing a prolate shape deformation, represented by the blue spheroids. The deformation causes the distance between the center of mass of the two bubbles to change from d(0) to d(t). In side view, the elongation is clearly visible because the direction of the induced deformation is parallel to the object plane of the side-view objective (*i.e.*, the x,y-plane). However, the top-view objective only reveals an x,z-plane projection of the deformation induced within a thin optical slice (see yellow bar). When the deviation from sphericity of this projection is below the resolution limit of the system, the bubble will still have a spherical appearance in top view. This explains why no deformation was observed in top view, even when bubbles were observed to move several hundred nanometers (Fig. 3).

In this study, a hydrodynamic point particle model including a restoring term $\vec{F}_k$ was used in a first attempt to capture the dynamics of interacting targeted microbubbles in response to ultrasound insonification. Although the predictive value of the model during and after ultrasound application (Figs. 8, 9) seemed to be satisfactory, several factors complicating the interpretation should be addressed. First, the bubbles are modeled as rigid spheres, moving parallel to the wall when subjected to secondary Bjerknes forces. Although this representation is what might be expected based on the top-view observations (Fig. 3), in fact bubbles are attached to the coated surface by means of a finite contact area, inducing a mechanical constraint, up to a point where the binding is ruptured. This configuration causes the bubbles to deform in the direction of the other bubble during ultrasound application, as revealed by side-view imaging, instead of translating as a sphere. The effect of the deformation on the magnitude of the hydrodynamic forces acting on the bubbles is not straightforward enough to quantify, which motivated us to use the approximate situation of translating spheres. In addition, the hydrodynamic model does not capture dissipative effects in the viscous boundary layer near the wall. The presence of a wall is known to influence the viscous dissipation experienced by a moving object (Leach et al. 2009; Ozarkar and Sangani, 2008). Neglecting these boundary effects is based on previous results on the translational dynamics of interacting bubbles in contact with, but not adherent to, a wall (Garbin et al. 2011). In that study, it was shown that the translational dynamics of these bubbles in response to ultrasound bursts could be predicted with good accuracy by a similar hydrodynamic model (but without the restoring term $\vec{F}_k$), also neglecting these boundary effects. We therefore assume that for our case, neglecting these effects in a first approximation is justified. Nevertheless, inclusion of the dissipative effects owing to the presence of the wall would probably improve the accuracy of the model and is currently under investigation.

The model can be improved further by the inclusion of force-dependent binding kinetics (Bell, 1978). A computational method combining large-scale hydrodynamics with stochastic molecular binding kinetics, known as *adhesive dynamics*, was shown to successfully predict experimentally observed phenomena associated with leukocyte adhesion, including rolling, transient attachment and firm adhesion (Hammer and Apte, 1992). The model also recreated the dynamics of leukocyte rolling over a functionalized surface under simple shear flow conditions successfully (Chang and Hammer, 2000). Recently, the adhesive dynamics model was applied to simulate the binding characteristics of single and dual-targeted microbubbles (Maul et al. 2010). However, these simulations were performed for bubbles subjected to simple steady shear flow, a situation that is different from a targeted microbubble subjected to an oscillatory acoustic attraction by a pulsating neighboring bubble.

We have presented a new method to determine the microbubble binding force using the mutual attraction between similarly sized targeted microbubbles. The net attractive force imposed on the bubble owing to the presence of the pulsating neighboring bubble induces a deformation of the bubble and the action of a restoring force $\vec{F}_k$, driving the recoil after the ultrasound is turned off. We hypothesize that the adhesion of a targeted microbubble to the functionalized substrate is ruptured when the restoring force $\vec{F}_k$ overcomes a certain threshold, which is the cumulative adhesive strength of the molecular interactions between bubble and substrate (*i.e.*, $\vec{F}_k > \Sigma \vec{F}_b$). By fitting the relaxation measurements with the hydrodynamic model after ultrasound application, a value for

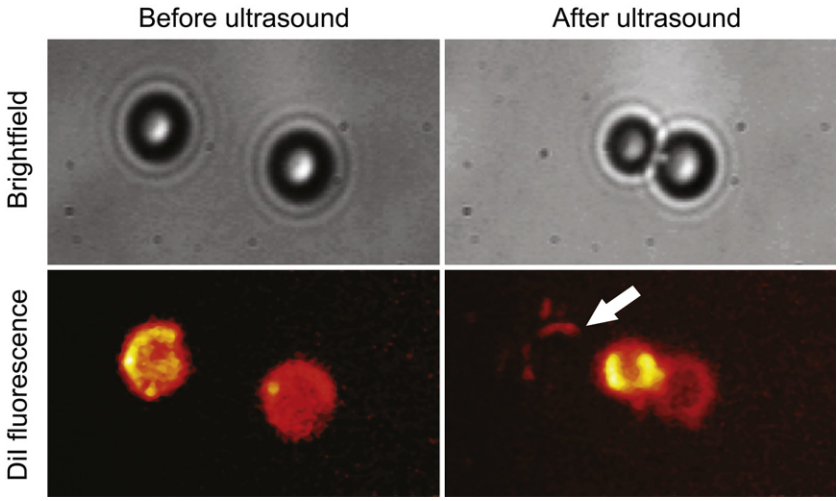

Fig. 11. The top row shows bright field images before (left) and after (right) ultrasound application. The bottom row shows corresponding DiI fluorescent images before (left) and after (right) ultrasound application. A semi-circular fluorescent patch (white arrow, indicative of lipids) remained at the initial binding site of the left bubble after detachment. The resting radii of the left and right bubbles are 2.1 and 2.0 μm, respectively.

the effective spring constant k could be obtained (Fig. 8). For a bubble with $R_0 = 2.1$ μm (bubble 1 in the inset of Fig. 6), the binding force with the surface was calculated to be 0.9–2.0 nN. From this binding force $\vec{F}_b$, an estimate of the number of molecular interactions between bubble and substrate can be derived, using the equation:

$$\vec{F}_b = \vec{f}_{\text{int}} N_{\text{int}} \tag{11}$$

where $\vec{f}_{\text{int}}$ is the strength of a single molecular interaction and N_{int} is the total number of bonds involved. The strength of a molecular bond (f_{int}) is known to be highly dependent on the applied loading rate (dF/dt; Evans and Ritchie, 1997; Merkel et al. 1999). The loading rate exerted on the bubbles (*i.e.*, multiple bonds) owing to the slow drift toward each other is in the order of 10^8 pN/s. Dependent on the number of bonds that are stressed just before detachment, the loading rate per molecular bond is expected to be in the range of 10^6–10^8 pN/s (*i.e.*, between 1–100 bonds involved). Traditional force probes such as the biomembrane force probe (BFP) and atomic force microscope (AFM) typically probe molecular bond strengths at significantly lower loading rates (i.e., 10^{-1} to 10^5 pN/s for BFP and 10^4 to 10^5 pN/s for AFM). Although no experimental data on molecular bond strength is available in the literature for the relatively high loading rates associated with the work presented here, we can make an order of magnitude estimate of the number of bonds involved.

The value of $\vec{f}_{\text{int}}$ in equation (11) depends on the locus of bond failure. The observation of patches of the fluorescent lipophilic dye DiI left at the initial binding site after microbubble detachment (Fig. 11) suggests that lipid anchors are pulled from the microbubble shell instead of biotin molecules unbinding from avidin. At a loading rate of 10^4 pN/s, the force needed to pull the lipid anchor of the DSPE-PEG2000-biotin molecule from a microbubble shell was measured to be ~35–45 pN, depending on the shell composition (Ounkomol et al. 2009). For comparison, the rupture force of the biotin-avidin interaction at similar loading rates was reported to be ~100 pN (Merkel et al. 1999). Lipid pullout therefore seems to be the weakest link and the most plausible locus of bond failure. As the strength of the lipid anchorage in the monolayer is expected to increase further with an increase in loading rate, dividing the measured binding force with $\vec{f}_{\text{int}}$ ~35–45 pN gives an upper limit of the number of bonds involved. Using equation (11), we get $N_{\text{int}} \sim$ 20–60 bonds. Most likely, molecular bonds throughout the contact zone between bubble and substrate will not be stressed uniformly during the unbinding process. Presumably, the molecular bonds at the distal margins of the adhesion zone will be stressed more and rupture first. When a certain threshold force is exceeded, the microbubble starts to detach from the functionalized substrate. The process then accelerates because of the ever-decreasing perimeter of the contact zone, a process best depicted as unzipping. Similarly, the threshold force for inducing cell mobility using shear flow has been ascribed to the properties of the molecular interactions at the trailing edge of the cell only (Garrivier et al. 2002).

The pressure threshold, above which the adhesion of the microbubbles is ruptured, depends on several factors. Shortening the pulse length will decrease the time during which the secondary Bjerknes force acts, and it is expected to increase the threshold. Insonifying the bubbles at higher frequencies away from resonance will also increase the threshold. The pressure threshold

is also affected by the adhesion strength between bubble and target surface. The biotin-avidin interaction used in this study is among the strongest non-covalent interactions in nature. Switching to a clinically relevant and biocompatible system (*e.g.*, ICAM-1 or VEGFR-2) makes the bonds much weaker, ultimately leading to a lower pressure threshold for microbubble detachment. Moreover, repetitive insonation of the targeted microbubbles with low-intensity ultrasound might induce bond fatigue, causing the bubbles to detach at lower pressures compared with bubbles insonified only once. In this study, the acoustic pressure was gradually increased until microbubble detachment was observed. Higher thresholds of detachment may be found when the bubbles are exposed to a single ultrasound burst only.

CONCLUSIONS

Targeted microbubbles subjected to secondary Bjerknes forces were observed to deform in the direction of their neighboring bubble, tending toward prolate spheroids. This deformation induces a restoring force driving the recoil observed after the ultrasound is turned off, typically occurring over $\sim$100 μs. At higher acoustic pressures, microbubbles were observed to detach from the functionalized substrate, a process in which the pullout of lipid anchors from the microbubble shell is likely involved. The dynamics of mutually interacting targeted microbubbles during and after ultrasound application were captured with reasonable accuracy by a simplified hydrodynamic point particle model. Based on this mutual attraction, we have proposed a new method to measure the microbubble binding force. For bubbles studied here, a binding force of 1–2 nN was found.

Acknowledgments—This work was supported by the Dutch Technology Foundation STW (project 10507). The authors thank F. Mastik for assistance with the Brandaris recordings; R. Beurskens, J. Honkoop, G. Springeling and M. Manten for their technical assistance; Dr. Ir. L. van Wijngaarden from the University of Twente for the fruitful discussions about bubble deformation; A.R. van der Wal for the valuable remarks on the manuscript; and Dr. A.L. Klibanov from the University of Virginia, Charlottesville, Virginia, USA, for providing information about microbubble fabrication.

SUPPLEMENTARY DATA

Supplementary data related to this article can be found online at http://dx.doi.org/10.1016/j.ultrasmedbio.2012.09.025.

REFERENCES

Bell GI. Models for the specific adhesion of cells to cells. Science 1978; 200:618–627.

Bjerknes V. Fields of force. New York: Colombia University Press; 1906.

Burns P, Powers J, Fritzsch T. Harmonic imaging: A new imaging and Doppler method for contrast enhanced ultrasound. Radiology 1992;185:142.

Chang KC, Hammer DA. Adhesive dynamics simulations of sialyl-Lewis(x)/E-selectin-mediated rolling in a cell-free system. Biophys J 2000;79:1891–1902.

Chin CT, Lancee C, Borsboom J, Mastik F, Frijlink ME, de Jong N, Versluis M, Lohse D. Brandaris 128: A digital 25 million frames per second camera with 128 highly sensitive frames. Rev Sci Instrum 2003;74:5026–5034.

Crum LA. Bjerknes forces on bubbles in a stationary sound field. J Acoust Soc Am 1975;57:1363–1370.

Dayton PA, Morgan KE, Klibanov AL, Brandenburger GH, Ferrara KW. Optical and acoustical observations of the effects of ultrasound on contrast agents. IEEE Trans Ultrason Ferroelectr Freq Control 1999;46:220–232.

de Jong N, Cornet R, Lancée CT. Higher harmonics of vibrating gas-filled microspheres. Part two: Measurements. Ultrasonics 1994;32: 455–459.

Deshpande N, Needles A, Willmann JK. Molecular ultrasound imaging: Current status and future directions. Clin Radiol 2010;65:567–581.

Dijkmans PA, Juffermans LJ, Musters RJ, van Wamel A, ten Cate FJ, van Gilst W, Visser CA, de Jong N, Kamp O. Microbubbles and ultrasound: from diagnosis to therapy. Eur J Echocardiogr 2004;5: 245–256.

Doinikov AA, Zhao S, Dayton PA. Modeling of the acoustic response from contrast agent microbubbles near a rigid wall. Ultrasonics 2009;49:195–201.

Evans E, Ritchie K. Dynamic strength of molecular adhesion bonds. Biophys J 1997;72:1541–1555.

Fritzsch T, Heldmann D, Weitschies W. Microparticle preparations made from biodegradable copolymers. World Patent WO 94/ 07539, 1994.

Garbin V, Cojoc D, Ferrari E, Di Fabrizio E, Overvelde MLJ, van der Meer SM, de Jong N, Lohse D, Versluis M. Changes in microbubble dynamics near a boundary revealed by combined optical micromanipulation and high-speed imaging. Appl Phys Lett 2007;90:114103.

Garbin V, Dollet B, Overvelde M, Cojoc D, Di Fabrizio E, van Wijngaarden L, Prosperetti A, de Jong N, Lohse D, Versluis M. History force on coated microbubbles propelled by ultrasound. Phys Fluids 2009;21:092003.

Garbin V, Overvelde M, Dollet B, de Jong N, Lohse D, Versluis M. Unbinding of targeted ultrasound contrast agent microbubbles by secondary acoustic forces. Phys Med Biol 2011;56:6161–6177.

Garrivier D, Decave E, Brechet Y, Bruckert F, Fourcade B. Peeling model for cell detachment. Eur Phys J E Soft Matter 2002;8:79–97.

Hammer DA, Apte SM. Simulation of cell rolling and adhesion on surfaces in shear flow: general results and analysis of selectin-mediated neutrophil adhesion. Biophys J 1992;63:35–57.

Klibanov AL, Hughes MS, Marsh JN, Hall CS, Miller JG, Wible JH, Brandenburger GH. Targeting of ultrasound contrast material. An in vitro feasibility study. Acta Radiol Suppl 1997;412:113–120.

Klibanov AL, Rasche PT, Hughes MS, Wojdyla JK, Galen KP, Wible JHJ, Brandenburger GH. Detection of individual microbubbles of ultrasound contrast agents: Imaging of free-floating and targeted bubbles. Invest Radiol 2004;39:187–195.

Landau E, Lifshitz. Fluid mechanics. 2nd edition. Oxford: Pergamon Press; 1987.

Leach J, Mushfique H, Keen S, Di Leonardo R, Ruocco G, Cooper JM, Padgett MJ. Comparison of Faxen's correction for a microsphere translating or rotating near a surface. Phys Rev E Stat Nonlin Soft Matter Phys 2009;79:026301.

Leighton T. The acoustic bubble. Waltham, MA: Academic Press; 1994.

Lotsberg O, Hovem JM, Aksum B. Experimental observation of subharmonic oscillations in Infoson bubbles. J Acoust Soc Am 1996;99: 1366–1369.

Marmottant P, van der Meer S, Emmer M, Versluis M, de Jong N, Hilgenfeldt S, Lohse D. A model for large amplitude oscillations of coated bubbles accounting for buckling and rupture. J Acoust Soc Am 2005;118:3499–3505.

Maul TM, Dudgeon DD, Beste MT, Hammer DA, Lazo JS, Villanueva FS, Wagner WR. Optimization of ultrasound contrast

agents with computational models to improve selection of ligands and binding strength. Biotechnol Bioeng 2010;107:854–864.
Merkel R, Nassoy P, Leung A, Ritchie K, Evans E. Energy landscapes of receptor-ligand bonds explored with dynamic force spectroscopy. Nature 1999;397:50–53.
Mor-Avi V, Caiani EG, Collins KA, Korcarz CE, Bednarz JE, Lang RM. Combined assessment of myocardial perfusion and regional left ventricular function by analysis of contrast-enhanced power modulation images. Circulation 2001;104:352–357.
Ohl CD, Tijink A, Prosperetti A. The added mass of an expanding bubble. J Fluid Mech 2003;482:271–290.
Ounkomol C, Xie H, Dayton PA, Heinrich V. Versatile horizontal force probe for mechanical tests on pipette-held cells, particles, and membrane capsules. Biophys J 2009;96:1218–1231.
Overvelde M, Garbin V, Dollet B, de Jong N, Lohse D, Versluis M. Dynamics of coated microbubbles adherent to a wall. Ultrasound Med Biol 2011;37:1500–1508.
Ozarkar SS, Sangani AS. A method for determining stokes flow around particles near a wall or in a thin film bounded by a wall and a gas-liquid interface. Phys Fluids 2008;20:063301.
Park EY, Smith MJ, Stropp ES, Snapp KR, DiVietro JA, Walker WF, Schmidtke DW, Diamond SL, Lawrence MB. Comparison of PSGL-1 microbead and neutrophil rolling: Microvillus elongation stabilizes P-selectin bond clusters. Biophys J 2002;82:1835–1847.
Pysz MA, Foygel K, Rosenberg J, Gambhir SS, Schneider M, Willmann JK. Antiangiogenic cancer therapy: Monitoring with molecular us and a clinically translatable contrast agent (BR55). Radiology 2010;256:519–527.
Rychak JJ, Lindner JR, Ley K, Klibanov AL. Deformable gas-filled microbubbles targeted to P-selectin. J Control Release 2006;114:288–299.
Schmidt BJ, Sousa I, van Beek AA, Bohmer MR. Adhesion and ultrasound-induced delivery from monodisperse microbubbles in a parallel plate flow cell. J Control Release 2008;131:19–26.
Sijl J, Dollet B, Overvelde M, Garbin V, Rozendal T, de Jong N, Lohse D, Versluis M. Subharmonic behavior of phospholipid-coated ultrasound contrast agent microbubbles. J Acoust Soc Am 2010;1285:3239–3252.
Simpson DH, Chin CT, Burns PN. Pulse inversion Doppler: A new method for detecting nonlinear echoes from microbubble contrast agents. IEEE Trans Ultrason Ferroelectr Freq Control 1999;46:372–382.
Straub JA, Chickering DE, Hartman TG, Gloff CA, Bernstein H. AI-700 pharmacokinetics, tissue distribution and exhaled elimination kinetics in rats. Int J Pharm 2007;328:35–41.
Takemura F, Magnaudet J. The history force on a rapidly shrinking bubble rising at finite Reynolds number. Phys Fluids 2004;16:3247–3255.
van der Meer SM, Dollet B, Voormolen MM, Chin CT, Bouakaz A, de Jong N, Versluis M, Lohse D. Microbubble spectroscopy of ultrasound contrast agents. J Acoust Soc Am 2007;121:648–656.
Vos HJ, Dollet B, Versluis M, de Jong N. Nonspherical shape oscillations of coated microbubbles in contact with a wall. Ultrasound Med Biol 2011;37:935–948.
Wijkstra H, Smeenge M, de la Rosette J, Pochon S, Tardy-Cantalupi I, Tranquart F. Targeted microbubble prostate cancer imaging with BR55. Abstract Book of the 17th European symposium on Ultrasound Contrast Imaging, January 19–20, Rotterdam, The Netherlands, 2012.
Willmann JK, Paulmurugan R, Chen K, Gheysens O, Rodriguez-Porcel M, Lutz AM, Chen IY, Chen X, Gambhir SS. US imaging of tumor angiogenesis with microbubbles targeted to vascular endothelial growth factor receptor type 2 in mice. Radiology 2008;246:508–518.

APPENDIX

In this article, we present the force balance for a targeted bubble translating in the x-direction because of an attractive secondary acoustic radiation force. In this force balance, a restoring force $\vec{F_k}$ was included to account for the recoiling observed after the ultrasound was turned off. The magnitude of this restoring force was assumed to be proportional to the position of the center of mass ($\vec{x_i}$) of the bubbles. In this appendix, we show that this assumption is indeed justified.

Simultaneous top- and side-view high-speed imaging revealed that a targeted bubble, subjected to an attractive secondary acoustic radiation force, deforms in the direction of the neighboring bubble, tending toward a prolate shape (see side-view images, Fig. 7). Figure 12 shows a schematic representation of this situation. The volume of a prolate ellipsoid is given by:

$$V = \frac{4}{3}\pi abc \tag{12}$$

where a, b and c are the semi-axes. If we assume that the bubble obtains a prolate spheroid shape (*i.e.*, $b=c$) and the deformation is volume conserving, we can state that:

$$V = \frac{4}{3}\pi ac^2 = \frac{4}{3}\pi R_s^3 \tag{13}$$

resulting in:

$$ac^2 = R_s^3 \tag{14}$$

where R_s is the radius of a sphere with equivalent volume. In case of a volume-conserving deformation, $R_s=R_0$. The surface area of a prolate spheroid is given by:

$$S = 2\pi c^2\left\{1+\frac{c}{ae}\arcsin e\right\} \tag{15}$$

where c is the semi-minor axis, a the semi-major axis and:

$$e^2 = 1-\frac{c^2}{a^2} = 1-\frac{R_s^3}{a^3} \tag{16}$$

Using equation (14) in combination with some simple algebra, equation (15) can be recast into:

$$S = 2\pi R_s^2\left\{\frac{R_s}{a}+\sqrt{\frac{a}{R_s}}\,\frac{\arcsin e}{e}\right\} \tag{17}$$

If e is small ($R_s \sim a$), we can write:

$$\frac{a}{R_s} = 1+\varepsilon \tag{18}$$

and:

$$S = 2\pi R_s^2\left\{(1-\varepsilon)+\left(1+\frac{1}{2}\varepsilon\right)^2\right\} \tag{19}$$

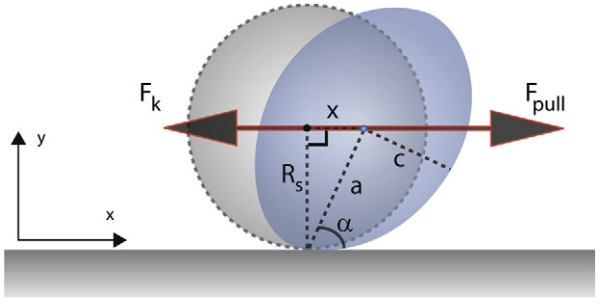

Fig. 12. A targeted bubble (grey circle) deforming toward a prolate spheroid (in blue) when subjected to an external pulling force (F_{pull}). F_{pull} is opposed by a restoring force F_k. R_s is the radius of the bubble, x is the translation of the center of mass, a and c are the semi-major and semi-minor axes of the spheroid, respectively, and α is the angle between a and the x-axis.

which can be reduced to:

$$S = 2\pi R_s^2 \left\{ 2 + \frac{1}{4}\varepsilon^2 \right\} \tag{20}$$

The work δW associated with a change δS in the surface area of a bubble is given by:

$$\delta W = \sigma\ \delta S \tag{21}$$

where σ is the effective surface tension of the microbubble. Differentiating equation (20) with respect to ε gives:

$$\frac{\delta S}{\delta \varepsilon} = \pi R_s^2 \varepsilon \tag{22}$$

Using equation (18), we can rewrite equation (22) as a function of a:

$$\frac{\delta S}{\delta a} = \pi\left(a - R_s\right) \tag{23}$$

Substituting equation (23) into equation (21) yields:

$$\delta W = \sigma\pi(a - \mathrm{R_s})\delta a \tag{24}$$

The amount of work δW needed to elongate the bubble by δa should result from the work of the external pulling force. The external pulling force can be decomposed in two components, one component parallel to a and one component orthogonal to a. The work needed to elongate the spheroid by δa is then provided by the parallel component only and can be calculated by:

$$\delta W = \mathrm{F_{pull}} \delta a\ cos\ \alpha \tag{25}$$

where α is the angle between a and the x-axis (Fig. 12). When the adhesion with the substrate is not disrupted, the pulling force (*i.e.*, the sum of all the relevant hydrodynamic forces) is opposed by the restoring force (*i.e.*, $F_{pull} = -F_k$). Combining equation (24) and equation (25) and substituting F_{pull} with $-F_k$ gives:

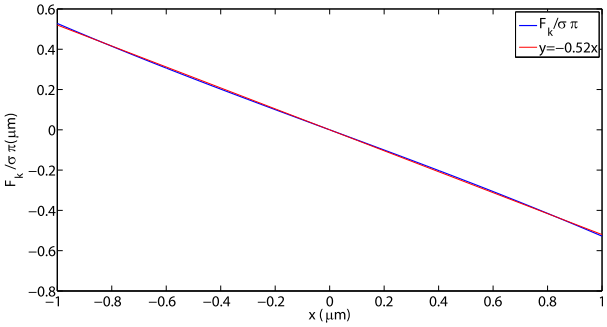

Fig. 13. Plot of the variation of the term $F_k/\sigma\pi$ with the displacement of the center of mass in the x-direction (blue curve). The best linear fit ($y = -0.52x$) is also plotted (red curve).

$$F_k = -\frac{\sigma\pi(a - R_s)}{\cos\ \alpha} \tag{26}$$

Substituting $\cos\alpha = x/a$, $a = \sqrt{x^2 + R_s^2}$ and some rearranging yields:

$$F_k = -\sigma\pi x - \sigma\pi \frac{R_s\left(R_s - \sqrt{x^2 + R_s^2}\right)}{x} \tag{27}$$

In Figure 13, the variation of the term $F_k/\sigma\pi$ with x plotted for the interval $-1\ \mu\mathrm{m} \leq x \leq 1\ \mu\mathrm{m}$. The linear relation $y = -0.52x$ gives a good overlap with the full equation on the interval relevant for the experiments described in this study, in which x typically varied from 0 to $\pm$ 0.5 μm. This shows that for the experiments presented here, the assumption of a linear relationship between the restoring force $\vec{F_k}$ and the position of the center of mass $\vec{x_i}$ is justified.